

Reachability Embeddings: Scalable Self-Supervised Representation Learning from Markovian Trajectories for Geospatial Computer Vision

Swetava Ganguli*[†]

C. V. Krishnakumar Iyer*

Vipul Pandey*

Abstract

Self-supervised representation learning techniques utilize large datasets without semantic annotations to learn meaningful, universal features that can be conveniently transferred to solve a wide variety of downstream supervised tasks. In this paper, we propose a self-supervised method for learning representations of geographic locations from unlabeled GPS trajectories to solve downstream geospatial computer vision tasks. Tiles resulting from a raster representation of the earth’s surface are modeled as nodes on a graph or pixels of an image. GPS trajectories are modeled as allowed Markovian paths on these nodes. A scalable and distributed algorithm is presented to compute image-like representations, called *reachability summaries*, of the spatial connectivity patterns between tiles and their neighbors implied by the observed Markovian paths. A convolutional, contractive autoencoder is trained to learn compressed representations, called *reachability embeddings*, of reachability summaries for every tile. Reachability embeddings serve as task-agnostic, feature representations of geographic locations. Using reachability embeddings as pixel representations for five different downstream geospatial tasks, cast as supervised semantic segmentation problems, we quantitatively demonstrate that reachability embeddings are semantically meaningful representations and result in 4–23% gain in performance, as measured using area under the precision-recall curve (AUPRC) metric, when compared to baseline models that use pixel representations that do not account for the spatial connectivity between tiles.

1 Introduction

1.1 Background Graphs are natural data structures for applications in diverse domains [28] e.g., recommendation systems, communication, social, and biological networks. Geospatial datasets (e.g., road networks, point clouds, 3D object meshes, GPS trajectories) can organically be represented as graphs with natural definitions of nodes and edges. Machine learning algorithms for graph analysis require feature vector representations of nodes, edges, substructures, or the whole graph. Instead of hand-engineering task-specific and domain-specific fea-

tures, recent methods [3] have focused on automatically learning low-dimensional, feature vector representations of graphs (*graph embeddings*) and their components (e.g., *node embeddings*).

In parallel, *self-supervised learning* (SSL) has been an area of active research and has achieved promising performance on both natural language processing (NLP) [2, 10, 32] and computer vision tasks [6, 23]. Bypassing the need for large, clean, labeled datasets which are expensive to produce in time and money, SSL often uses predefined *pretext tasks* to derive supervision signals directly from unlabeled data by making neural networks predict withheld parts or properties of inputs. SSL aims to learn semantically meaningful, task-agnostic representations of data that can be used as inputs by downstream (usually supervised) task-specific models. SSL has been used to learn context-independent [32] and contextual [2, 10], task-agnostic word embeddings for NLP applications. Most popular SSL techniques for learning visual representations can be classified into two types: *generative* approaches that learn representations under the *pretext* of generating images by modeling the data distribution [12, 27, 19], and *discriminative* approaches that use *pretext tasks*, designed to efficiently produce labels for inputs (e.g., based on heuristics [11, 17, 34] or contrastive learning [6, 23]), coupled with a supervised objective.

Geospatial computer vision research has largely focused on active (e.g., SAR) and passive (e.g., optical) imagery data [15, 31, 37]. This paper proposes a novel technique to make privacy-preserving GPS trajectories, which are sequential, spatiotemporal datasets with rich geospatial connectivity information, amenable to computer vision-based analysis by itself or in combination with other data modalities. GPS and mobility datasets have been used for diverse applications [8] including transportation modeling [50], public safety and health policy [41], and building mapping services [24, 48].

1.2 Present Work and Contributions We present a novel self-supervised method for learning task-agnostic feature representations of geographic locations from GPS trajectories by modeling tiles resulting from a raster rep-

*Apple, Cupertino, CA. {swetava, cvk, vipul}@apple.com.

[†]Corresponding Author. Also: swetava@cs.stanford.edu.

resentation of the earth’s surface as nodes of a graph (termed *earth surface graph* (ESG)) and modeling the *observed* GPS trajectories as evidence of *allowed* Markovian paths on this graph. Equivalently, the proposed method learns node embeddings, for all nodes in the ESG, from observed paths on the ESG. The proposed method has two stages. The first stage (Sections 4.1–4.4) generates an *image-like* representation, termed *reachability summary*, for nodes using observed trajectories passing through the node, during a predefined observation time interval, Δt . A scalable and distributed algorithm is proposed for the first stage. The second stage (Section 4.5) generates d_R -dimensional, compressed representations from reachability summaries, called *reachability embeddings*, using a fully-convolutional, contractive autoencoder. In Section E of Supplementary Materials, reachability embeddings are theoretically motivated and interpreted using the Chapman-Kolmogorov equations for Markov chains.

Experiments in Section 6 evaluate the impact of reachability embeddings on solving downstream geospatial computer vision tasks using supervised semantic segmentation. The model inputs are combinations of image-like derivatives of road network and GPS trajectory data (Section 5) with pixels corresponding to nodes (convenient by design) of the ESG. For five different downstream tasks, we show that using reachability embeddings as input features outperforms baselines (models with input features that do not account for spatial connectivity between nodes) resulting in 4–23% gain in AUPRC (area under precision-recall curve) while requiring upto 67% less trajectory data than the baselines. Thus, reachability embeddings are semantically meaningful representations of geographic locations and denser, more informative representations derived from trajectories compared to those not accounting for spatial connectivity between nodes.

Presence of geospatial features (e.g., traffic control devices, parking lots, overpasses) at a location, ℓ , imposes constraints on traffic flow that manifests in the (i) frequency of, (ii) directionality (from or to ℓ) of, (iii) time taken during, and (iv) distance traveled during observed transitions between ℓ and its neighbors across various motion modalities (e.g., walking, driving, biking). Reachability summaries, and consequently reachability embeddings, are designed to be *contextual* representations (analogous to advantage of contextual [10] over fixed [32] word embeddings in NLP) that encode these motion characteristics and traffic flow patterns occurring during Δt . Events that significantly change traffic patterns like road construction, road closures, seasonal effects, etc. change the computed embeddings making them a good input feature candidate for geospatial fea-

ture or change detection models. In contrast to digital images, where pixel values are a convenient mathematical representation of an underlying object or scene, reachability summaries are 2D, spatial-relation-preserving transition frequency matrices cast in an image-like format to make them amenable to computer vision-based analysis. Hence, existing discriminative methods (heuristic or contrastive) are not natural self-supervision tasks to learn representations from reachability summaries. Instead, reconstruction with contractive regularization [39], which incentivizes robustness of embeddings by encouraging invariance to small perturbations of the reachability summary, is used as the self-supervision signal.

While the presentation in this paper is targeted towards geospatial and remote sensing applications, the concept of generating node embeddings based on reachability can be extended to graphs in other domains. For example, (i) graph traversal algorithms can be used to assemble node reachability summaries; (ii) sampled random walk paths, used in [13, 22, 38], can be used analogous to trajectories to compute reachability summaries for nodes. The generated summaries can be subsequently encoded into reachability embeddings.

2 Related Work

Graph Node Embeddings: Existing deep learning methods for generating node embeddings of a *known* graph follow three distinct themes [3]: (a) using NLP-inspired methods like skip-gram [13, 22, 38] or RNNs [30] to process *sampled* random walk paths from a graph similar to sequences; (b) compressing matrix representations [5, 45] derived from graphs; (c) using graph neural networks and its variants [51]. In contrast, our framework reconstructs image-like reachability summaries, derived from *observed* trajectories, for nodes in an *inferred* directed graph (ESG) to generate node embeddings.

SSL for Computer Vision: SSL has been successfully applied to learn effective visual representations [26, 29]. Generative methods learn representations by modeling the data distribution [12, 19, 27] or reconstructing the input or feature [18, 21, 44]. Examples of heuristic, discriminative pretext tasks used to learn representations include context prediction [11], solving jigsaw puzzles of image patches [34], and predicting image rotations [17]. Among discriminative methods, contrastive methods currently achieve state-of-the-art performance in SSL [23, 6]. Reachability summary generation and its contractive reconstruction can together be viewed as the generative pretext task that encodes the co-occurrence relationships inherent in geospatial transitions (resulting from interaction of traffic and local transport infrastructure) to obtain reachability embeddings.

GPS Trajectory Embeddings: Most existing meth-

ods using GPS record or trajectory representations process trajectories similar to sequences with NLP-inspired methods like skip-gram or RNNs e.g., location similarity prediction [7], motion modality classification [9, 25, 16], demographic attribute prediction [42], and living pattern recognition [4]. To the best of our knowledge, no prior work uses the Markovian concept of reachability and a computer vision-based SSL pretext task to learn self-supervised, contextual representations of geographic locations.

3 Notation and Preliminaries

Figure 1 provides a reference schematic for notation and terminology introduced in this and the next section.

DEFINITION 3.1. A **zoom- q tile** is the cell or tile resulting from a $2^q \times 2^q$ raster representation of the spherical Mercator projection of the earth’s surface [14]. With the northwest corner tile as origin, every tile, \mathbf{s} , is assigned 2D, non-zero integer coordinates, $(\mathbf{x}_s, \mathbf{y}_s)$, which increase in the \mathbf{x} -direction towards the east (right) and in the \mathbf{y} -direction towards the south (down).

DEFINITION 3.2. A **GPS trajectory**, $\mathbf{T}_i \in \mathcal{T}(t_0, \Delta t)$, or simply **trajectory**, is a discrete, sequential, and chronological representation of the spatiotemporal movement of an object [50] consisting of sequence of ordered pairs, $\mathbf{T}_i = \{\mathbf{p}_1^i, \dots, \mathbf{p}_{n_i}^i\}$, where pair, $\mathbf{p}_k^i = \{\mathbf{z}_k^i, \mathbf{t}_k^i\}$, for $k = 1, \dots, n_i$. \mathbf{p}_k^i is called a **GPS record**¹ or simply a **record**. $\mathcal{T}(t_0, \Delta t)$ is the set of $|\mathcal{T}(t_0, \Delta t)| = M$ trajectories occurring within observation time interval, Δt , starting at t_0 , n_i is length of trajectory \mathbf{T}_i , and \mathbf{z}_k^i is the zoom-24 tile² where the object with trajectory \mathbf{T}_i was present at time \mathbf{t}_k^i . Note: $\mathbf{t}_1^i < \dots < \mathbf{t}_{n_i}^i$ for $i = 1, \dots, M$.

DEFINITION 3.3. The **implied allowed transitions multiset**, \mathbf{A}_i^m , associated with trajectory \mathbf{T}_i is the unordered multiset of all ${}^{n_i}P_2 = n_i(n_i - 1)$ ordered pairs of zoom-24 tiles, $\{\mathbf{z}_k, \mathbf{z}_l\}$, that can be constructed from trajectory \mathbf{T}_i such that $l \geq k$. The unordered set consisting of only the unique ordered pairs is denoted as \mathbf{A}_i^s and called the **implied allowed transitions set**.

Ordered pairs generated from the trajectories are modeled as Markovian state transitions over the countably finite state space of zoom-24 tiles. Hence, the trajectory index is dropped from the the ordered pairs in def. (3.3).

DEFINITION 3.4. The **earth surface graph (ESG)**, $\mathbf{G}_{ES}(\mathbf{V}_{ES}, \mathbf{E}_{ES})$, is a weighted directed graph representation of the earth’s surface where zoom-24 tiles

¹Finite area tiles mitigate handling real-valued latitude-longitude pairs. The tile represents all such pairs within itself.

²Corresponds to spatial resolution $\approx 2.38\text{m}$ at the equator.

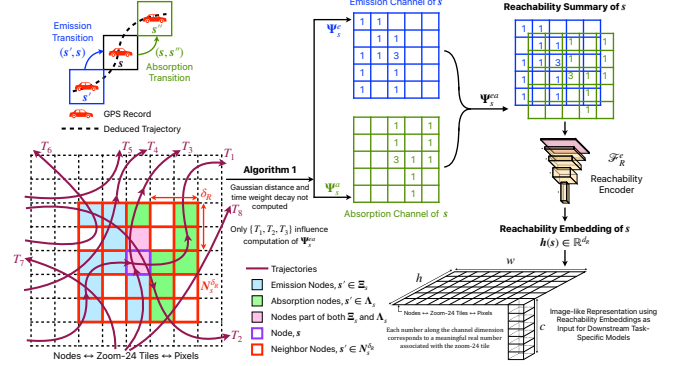


Figure 1: Schematic describing reachability embeddings.

form the nodes, \mathbf{V}_{ES} , and the set union of \mathbf{A}_i^s of all $\mathbf{T}_i \in \mathcal{T}(t_0, \Delta t)$ forms the edge set, \mathbf{E}_{ES} . For nodes, $\mathbf{s}, \mathbf{s}' \in \mathbf{V}_{ES}$, $\mathbf{c}_i^{(\mathbf{s}, \mathbf{s}')}$ is the number of occurrences of the transition $(\mathbf{s}, \mathbf{s}')$ in \mathbf{A}_i^m . The directed edge, $(\mathbf{s}, \mathbf{s}')$, in \mathbf{E}_{ES} is assigned the weight, $\mathbf{w}_{ES}^{(\mathbf{s}, \mathbf{s}')} = \sum_{i=1}^M \mathbf{c}_i^{(\mathbf{s}, \mathbf{s}')}$.

Definitions (3.2), (3.3), and (3.4) present the equivalences used in this paper: (i) zoom-24 tiles \leftrightarrow Markovian state space $\mathbf{V}_{ES} \leftrightarrow$ nodes of \mathbf{G}_{ES} , (ii) GPS trajectory \leftrightarrow Markovian trajectory in $\mathbf{V}_{ES} \leftrightarrow$ path on \mathbf{G}_{ES} .

DEFINITION 3.5. Given two nodes, $\mathbf{s}_1, \mathbf{s}_2 \in \mathbf{V}_{ES}$, \mathbf{s}_2 is **reachable** from \mathbf{s}_1 if $\exists (\mathbf{s}_1, \mathbf{s}_2) \in \mathbf{E}_{ES}$.

While $q = 24$ in this paper, the algorithms presented in Section 4, are generic and treat q as a parameter.

4 Methodology

4.1 Reachability Embeddings The proposed method learns a mapping function, $\mathbf{f}_R : \mathbf{V}_{ES} \rightarrow \mathbb{R}^{d_R}$, from nodes in the ESG, \mathbf{V}_{ES} , to real valued, d_R -dimensional feature representations we call reachability embeddings. Each record in a trajectory is associated with a motion modality (e.g., driving, walking, biking). A pre-trained, LSTM-based, neural motion modality filter is used to keep only the records corresponding to a chosen modality. Henceforth, we will assume that all records in all trajectories in $\mathcal{T}(t_0, \Delta t)$ have the same motion modality.

Given a node, $\mathbf{s} \in \mathbf{V}_{ES}$, two sets of nodes can naturally be defined relative to \mathbf{s} based on observed reachability patterns in trajectories in $\mathcal{T}(t_0, \Delta t)$. The first set, called the **emission set** for node \mathbf{s} , $\mathbf{\Xi}_s$, consists of nodes *from which* transitions to \mathbf{s} are observed. Such transitions are termed **emission transitions**. The second set, called the **absorption set** for node \mathbf{s} , $\mathbf{\Lambda}_s$, consists of nodes *to which* transitions from \mathbf{s} are observed. Such transitions are termed **absorption transitions**. Thus,

$$\mathbf{\Xi}_s := \{ \mathbf{s}' \mid \mathbf{s}' \in \mathbf{V}_{ES} \text{ and } (\mathbf{s}', \mathbf{s}) \in \mathbf{E}_{ES} \}, \quad (4.1a)$$

$$\mathbf{\Lambda}_s := \{ \mathbf{s}' \mid \mathbf{s}' \in \mathbf{V}_{ES} \text{ and } (\mathbf{s}, \mathbf{s}') \in \mathbf{E}_{ES} \}. \quad (4.1b)$$

Owing to transitions from \mathbf{s} to itself, $\mathbf{s} \in \Xi_s, \Lambda_s$. With the intuition that transitions occurring over large spatial distances should not influence the learned representations of nodes, transitions occurring only within a specified buffer, termed the *reachability buffer*, $\delta_R \in \mathbb{Z}^+$, are considered valid. The set of nodes within δ_R of node \mathbf{s} , called the *reachable neighborhood*, $\mathbf{N}_s^{\delta_R}$, are

$$\mathbf{N}_s^{\delta_R} := \{ \mathbf{s}' \mid \mathbf{s}' \in \mathbf{V}_{ES}, |\mathbf{x}_s - \mathbf{x}_{s'}| \leq \delta_R, |\mathbf{y}_s - \mathbf{y}_{s'}| \leq \delta_R \}. \quad (4.2)$$

Combining definitions (4.1a), (4.1b), and (4.2), the set of valid emission and absorption transitions with respect to node \mathbf{s} , denoted as $\Xi_s^{\delta_R}$ and $\Lambda_s^{\delta_R}$ respectively, are

$$\Xi_s^{\delta_R} = \Xi_s \cap \mathbf{N}_s^{\delta_R} \quad \text{and} \quad \Lambda_s^{\delta_R} = \Lambda_s \cap \mathbf{N}_s^{\delta_R}. \quad (4.3)$$

The Cartesian grid structure of nodes in \mathbf{V}_{ES} can be exploited to create an *image-like* representation of the reachability pattern for all nodes, \mathbf{s} , implied by their $\Xi_s^{\delta_R}$ and $\Lambda_s^{\delta_R}$. With $\mathbf{L} = 2\delta_R + 1$, for each $\mathbf{s} \in \mathbf{V}_{ES}$, construct two zero-initialized $\mathbf{L} \times \mathbf{L}$ square matrices, Ψ_s^e (*emission channel*) and Ψ_s^a (*absorption channel*), with the top-left corner entries assigned the index $(0, 0)$, first index increasing rightward, and second index increasing downward. For every $\mathbf{s}' \in \Xi_s^{\delta_R}$ and $\mathbf{s}'' \in \Lambda_s^{\delta_R}$, set

$$\Psi_s^e[\mathbf{x}_{s'} - \mathbf{x}_s + \delta_R, \mathbf{y}_{s'} - \mathbf{y}_s + \delta_R] = \mathbf{w}_{ES}^{(s',s)} \quad (4.4a)$$

$$\Psi_s^a[\mathbf{x}_{s''} - \mathbf{x}_s + \delta_R, \mathbf{y}_{s''} - \mathbf{y}_s + \delta_R] = \mathbf{w}_{ES}^{(s,s'')} \quad (4.4b)$$

The (δ_R, δ_R) -indexed entry equals $\mathbf{w}_{ES}^{(s,s)}$ in both, Ψ_s^e and Ψ_s^a . Matrices Ψ_s^e and Ψ_s^a , have two important properties: (i) they preserve the relative spatial proximity of nodes in $\mathbf{N}_s^{\delta_R}$ with respect to \mathbf{s} ; (ii) normalization by matrix sums yields the Markovian transition probabilities to \mathbf{s} from all $\mathbf{s}' \in \mathbf{N}_s^{\delta_R}$ and from \mathbf{s} to all $\mathbf{s}'' \in \mathbf{N}_s^{\delta_R}$, respectively. Matrices, Ψ_s^e and Ψ_s^a , are treated as two channels and stacked along the channel dimension to create a $\mathbf{L} \times \mathbf{L} \times 2$ -dimensional, image-like entity, called the *reachability summary*, Ψ_s^{ea} , for node \mathbf{s} . A contractive [39], fully-convolutional autoencoder, \mathcal{F}_R , is trained to generate compressed, robust, low-dimensional representations of Ψ_s^{ea} , called the *reachability embedding*, $\mathbf{h}(\mathbf{s}) \in \mathbb{R}^{d_R}$, for node \mathbf{s} using contractive reconstruction of Ψ_s^{ea} as the self-supervision task for representation learning. Reachability embeddings, produced for every node $\mathbf{s} \in \mathbf{V}_{ES}$ by employing the encoder component of \mathcal{F}_R , captures the spatial connectivity of node \mathbf{s} to nodes in $\mathbf{N}_s^{\delta_R}$ as evidenced by observed trajectories (modeled as Markovian) in $\mathcal{T}(t_0, \Delta t)$.

4.2 Distributed data-parallel algorithm for generating reachability summaries Computing Ψ_s^{ea} for all $\mathbf{s} \in \mathbf{V}_{ES}$ requires analysing all M trajectories in $\mathcal{T}(t_0, \Delta t)$ and computing upto 2^{2q} matrices of size

$\mathbf{L} \times \mathbf{L} \times 2$, where $q = 24$. In practice, however, given a choice of motion modality, only a subset (e.g., no driving or walking on water bodies) of the zoom-24 tiles (called *active tiles* and denoted as $\overline{\mathbf{V}}_{ES}$) have trajectories that pass through them. The embedding vector is set to zero for non-active tiles. Algorithm 1 proposes an efficient method to compute $\Psi_s^{ea} \forall \mathbf{s} \in \overline{\mathbf{V}}_{ES}$ from $\mathcal{T}(t_0, \Delta t)$ assuming all its trajectories are of the same, user-chosen motion modality. The key idea in Algorithm 1 is to compute $\mathbf{w}_{ES}^{(s_1, s_2)}$, $\mathbf{s}_1, \mathbf{s}_2 \in \overline{\mathbf{V}}_{ES}$ for all unique $(\mathbf{s}_1, \mathbf{s}_2)$ pairs (emission and absorption transitions) independently in parallel and then assemble the dense tensor, Ψ_s^{ea} , for each $\mathbf{s} \in \overline{\mathbf{V}}_{ES}$. For node \mathbf{s} , let $\mathbf{S}_s^a : r_s(\mathbf{s}') \rightarrow c_s^a(\mathbf{s}')$ be a map constructed from observed absorption transitions $(\mathbf{s}, \mathbf{s}')$ for $\mathbf{s}' \in \mathbf{N}_s^{\delta_R}$. Here, $r_s(\mathbf{s}')$ is the row-major index of \mathbf{s}' in Ψ_s^a and $c_s^a(\mathbf{s}')$ is the frequency of observing the transition $(\mathbf{s}, \mathbf{s}')$, which equals $\mathbf{w}_{ES}^{(s, s')}$ when Algorithm 1 finishes. Analogously, define $\mathbf{S}_s^e : r_s(\mathbf{s}') \rightarrow c_s^e(\mathbf{s}')$ with $c_s^e(\mathbf{s}')$ being frequency of observing transition $(\mathbf{s}', \mathbf{s})$ which equals $\mathbf{w}_{ES}^{(s', s)}$ when algorithm 1 finishes. The reachability map, $\mathbf{S} : \mathbf{s} \rightarrow \{\mathbf{S}_s^e, \mathbf{S}_s^a\}$, is a map from each node $\mathbf{s} \in \overline{\mathbf{V}}_{ES}$ to the tuple of the node's emission and absorption transition maps, \mathbf{S}_s^e and \mathbf{S}_s^a . \mathbf{S}_s^e and \mathbf{S}_s^a are sparse representations of the information required to assemble Ψ_s^e and Ψ_s^a (or equivalently Ψ_s^{ea}). The pseudo-code of a distributed data-parallel implementation of Algorithm 1 using the Apache Spark framework is provided in Section A of Supplementary Materials.

4.3 Capturing more than spatial connectivity

in $\Psi_s^e, \Psi_s^a, \Psi_s^{ea}$ The emission (Ψ_s^e) and absorption (Ψ_s^a) channels, as defined in Section 4.1, capture only the spatial connectivity between two nodes. In Algorithm 1, if the transition $(\mathbf{s}, \mathbf{s}')$, with $\mathbf{s}' \in \mathbf{N}_s^{\delta_R}$, is observed in trajectory \mathbf{T}_i , $\Psi_s^a(\mathbf{s}')$ and $\Psi_{s'}^e(\mathbf{s})$ are both incremented by 1. These increments, denoted as $\Delta\Psi_s^a(\mathbf{s}')$ and $\Delta\Psi_{s'}^e(\mathbf{s})$, are independent of the distance covered, $\Delta_{d,i}^{(s, s')}$, or time taken, $\Delta_{t,i}^{(s, s')} = \mathbf{t}_{s'}^i - \mathbf{t}_s^i$, to reach \mathbf{s}' from \mathbf{s} in trajectory \mathbf{T}_i , noting that time taken and distance covered depend on the trajectory if multiple paths between the two nodes exist. Gaussian weight decay is used to incorporate this information into $\Psi_s^a(\mathbf{s}')$ and $\Psi_{s'}^e(\mathbf{s})$. The Gaussian with parameters μ and σ is $G(\mu, \sigma) = (1/\sqrt{2\pi}\sigma)e^{-\mu^2/2\sigma^2}$. Given σ_d and σ_t , two user-supplied hyperparameters that control the strengths of the distance and time weight decays, respectively, the weighted increment in $\Psi_s^a(\mathbf{s}')$ and $\Psi_{s'}^e(\mathbf{s})$ associated with the transition $(\mathbf{s}, \mathbf{s}')$ in trajectory \mathbf{T}_i , is $\Delta\Psi_s^a(\mathbf{s}') = \Delta\Psi_{s'}^e(\mathbf{s}) := \Delta\mathbf{w}(\mathbf{s}, \mathbf{s}'; \sigma_d, \sigma_t) = G(\Delta_{d,i}^{(s, s')}, \sigma_d) \cdot G(\Delta_{t,i}^{(s, s')}, \sigma_t)$. A modified `analyzeTrajectories` procedure for Algorithm 1 implementing the equation above is presented in Algorithm 3 in Section B of the Supplementary Materials.

4.4 Scalability of Algorithm 1 Algorithm 1 modified using Algorithm 3 is implemented using the Scalabased, Spark Dataset API. To demonstrate scalability, the publicly available T-Drive dataset [49] is suitably pre-processed (detailed in Supplementary Materials Section C) to obtain three datasets of 2000, 8000, and 64000 trips on which strong scaling [20] analysis is performed.

Algorithm 1 Generate Ψ_s^{ea} for all nodes $s \in \bar{V}_{ES}$

Input: $\mathcal{T}_{t_0}^{t_0+\Delta t} = \{T_1 \dots T_M\}$, $|T_i| = n_i \forall i \in [1, M]$,

$T_i = \{p_1^i, \dots, p_{n_i}^i\}$ where $p_k^i = \{z_k^i, t_k^i\}$

Output: Map $\Psi : s \rightarrow \Psi_s^{ea}$

Parameters: δ_R . Define $L = 2\delta_R + 1$

procedure ReachabilitySummaryGenerator()

Initialize map $\Psi = \emptyset$

$S \leftarrow \text{analyzeTrajectories}(\mathcal{T}_{t_0}^{t_0+\Delta t})$

for node $s \in S$ **do**

Arrays Ψ_s^e, Ψ_s^a . Zero-initialized of length L^2

$S_s^e, S_s^a \leftarrow S[s]$

$\Psi_s^e[\kappa] = S_s^e[\kappa]$ **for all** keys κ of map S_s^e

$\Psi_s^a[\kappa] = S_s^a[\kappa]$ **for all** keys κ of map S_s^a

Reshape Ψ_s^e and Ψ_s^a to $L \times L$ arrays

$\Psi_s^{ea} \leftarrow \text{Stack channels } \Psi_s^e, \Psi_s^a$

$\Psi[s] \leftarrow \Psi_s^{ea}$

function analyzeTrajectories($\mathcal{T}_{t_0}^{t_0+\Delta t}$)

Initialize map $S = \emptyset$

for trajectory $T_i \in \mathcal{T}_{t_0}^{t_0+\Delta t}$ **do**

for $k \leftarrow 1$ to n_i **do**

for $l \leftarrow k$ to n_i **do**

if $z_k^i \in N_{z_k^i}^{\delta_R}$ **then**

if $z_k^i \notin S$, $S[z_k^i] = \{S_{z_k^i}^e = S_{z_k^i}^a = \emptyset\}$

if $z_l^i \notin S$, $S[z_l^i] = \{S_{z_l^i}^e = S_{z_l^i}^a = \emptyset\}$

$r_{z_k^i}(z_l^i) \leftarrow \text{getIndex}(z_k^i, z_l^i)$

$r_{z_l^i}(z_k^i) \leftarrow \text{getIndex}(z_l^i, z_k^i)$

$c_{z_k^i}^a(z_l^i) = c_{z_l^i}^e(z_k^i) = 1.0$

$S_{z_k^i}^a[r_{z_k^i}(z_l^i)] += c_{z_l^i}^a(z_k^i)$

$S_{z_l^i}^e[r_{z_l^i}(z_k^i)] += c_{z_k^i}^e(z_l^i)$

return S

function getIndex(s, s')

return $L(y_{s'} - y_s + \delta_R) + (x_{s'} - x_s + \delta_R)$

Algorithm 1 is executed on these datasets by varying number of CPU cores from 10 to 2000. The mean value of the runtime and strong scaling efficiency³ [20] obtained over seven runs is plotted in Figures 2a and 2b, respectively, as the number of CPU cores are varied

³For a given dataset size, if t_c^{id} is the ideal time required on c , $t_{c_0}^m$ is the time measured when executing algorithm on c_0 cores, and e_{ss} is strong scaling efficiency, then $t_c^{\text{id}} = t_{c_0}^m(c_0/c)$ and $e_{ss} = t_c^{\text{id}}/t_{c_0}^m$.

for the three datasets. Typical characteristics of parallel applications such as increased efficiency on larger number of cores for bigger problem sizes, efficiency drop for smaller problem sizes as number of cores increases, and communication latency dominating compute time are observed.

Another scalability test is to increase the number of trajectories processed by algorithm 1 on a fixed number of cores. Plotting the runtime of Algorithm 1 as the number of trajectories are varied from 1000 to 64000 and the number of cores are varied from 10 to 100 in Figure 2c, it is empirically observed that the algorithm run-time scales sub-linearly with the number of trajectories with a power law exponent of roughly 1/5. While Figure 2 and the observations in this subsection are stated specifically for the T-Drive dataset, similar observations are empirically observed on much larger proprietary datasets (described in section 5). Scalability of Algorithm 1 is especially crucial in a setting where embeddings need to be generated periodically for maintaining and updating geospatial maps given the large number of zoom-24 tiles that are possible on the surface of the earth. Contrast this to vocabulary sizes ($\mathcal{O}(10^6)$) used in NLP approaches like word2vec [32].

4.5 Encoding reachability summaries The neural architecture of the fully-convolutional, contractive autoencoder, \mathcal{F}_R , is shown in Figure 4 of Section D of the Supplementary Materials. During training, the encoder, \mathcal{F}_R^e , maps Ψ_s^{ea} to a compressed representation, $\mathbf{h}(s) = \mathcal{F}_R^e(\Psi_s^{ea}) \in \mathbb{R}^{d_R}$, which is then used by the decoder, \mathcal{F}_R^d , to reconstruct Ψ_s^{ea} . The objective function to be minimized, \mathcal{L} , consists of the reconstruction loss, \mathcal{L}_{rec} , regularized by the contractive loss, \mathcal{L}_{con} , shown in equations (4.5a), (4.5b), and (4.5c).

$$\mathcal{L}_{rec}(\mathbf{s}; \boldsymbol{\theta}) = \|\Psi_s^{ea} - \mathcal{F}_R^d(\mathcal{F}_R^e(\Psi_s^{ea}))\|_2^2 \quad (4.5a)$$

$$\mathcal{L}_{con}(\mathbf{s}; \boldsymbol{\theta}) = \sum_{i=0}^{d_R-1} \|\nabla_{\Psi_s^{ea}} \mathbf{h}_i(\mathbf{s})\|_2^2 \quad (4.5b)$$

$$\mathcal{L}(\boldsymbol{\theta}) = \mathbb{E}_{s \sim \bar{V}_{ES}} [\mathcal{L}_{rec}(\mathbf{s}; \boldsymbol{\theta}) + \lambda \mathcal{L}_{con}(\mathbf{s}; \boldsymbol{\theta})] \quad (4.5c)$$

Here, $\boldsymbol{\theta}$ are the parameters of \mathcal{F}_R and λ is a hyperparameter. A ReLU nonlinearity forces all embeddings to be positive real vectors. Since there is no upper bound on the pixel values in Ψ_s^{ea} , the input to \mathcal{F}_R is log-normalized and the reconstruction output exponentiated (similar to [48]) before calculating the losses (4.5a)–(4.5c) to train the neural network stably and avoid spurious effects from the large dynamic range of Ψ_s^{ea} . The training set is composed of zoom-24 tiles from a variety of geographically diverse regions. Once trained, \mathcal{F}_R^e is used to generate the embeddings, $\mathbf{h}(s)$, for all $s \in \bar{V}_{ES}$. As shown in [39], contractive regularization forces $\mathbf{h}(s)$ to be invariant to

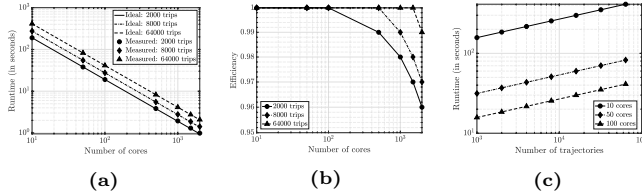


Figure 2: Strong scaling analysis of (a) runtime, (b) efficiency, and (c) scaling with number of trajectories of Algorithm 1.

small perturbations of Ψ_s^{ea} (locally contractive in neighborhood of Ψ_s^{ea}) thereby yielding robust, compressed representations of Ψ_s^{ea} . Presence of \mathcal{L}_{con} yields only a few non-zero elements in the embeddings for most nodes. From the perspective of energy-based models, \mathcal{L}_{con} helps minimize the volume of low-energy regions to help learn semantically meaningful representations.

5 Dataset Description

Small, publicly available GPS trajectory datasets (e.g., [33],[35],[49]) (i) have varying sampling rates with incomplete trajectories, (ii) do not cover the entire road network in the geographical areas they are obtained from, (iii) have inconsistent observation times and intervals, and (iv) lack geographical diversity. Most importantly, in order to test the utility of learned unsupervised representations like reachability embeddings on downstream supervised tasks, we need labeled data for these tasks. To the best of our knowledge, there is no sufficiently large, geographically diverse, publicly available, privacy-preserving GPS trajectory dataset covering a sufficiently large observation time interval which can be matched to labeled datasets collected for various geospatial tasks in the same geographical regions.

To overcome this difficulty, we use *probe data* [36], which is a privacy-preserving, structured, sequential, and proprietary dataset⁴. Labels are collected across a variety of geographic regions, in the form of *Well-Known Text* (WKT) polygons⁵ [47], for training supervised semantic segmentation models for five downstream geospatial tasks described in Section 6.

There are multiple ways, called *local aggregate representations* (LAR), simpler than reachability embeddings, to create semantically meaningful, multi-channel, *image-like* representations of GPS trajectory datasets making them amenable for use by downstream computer vision models for geospatial tasks. The pixel values for a given zoom-24 tile are obtained by analyzing records observed *only in that tile* (local) to yield one (single-channel) or

a vector of aggregate counts (multi-channel). Three such representations are count-based raster map (CRM), heading count-based raster map (HCRM), and speed count (SC).

Given the Cartesian grid structure of \mathbf{V}_{ES} , associating \mathbf{c} meaningful real numbers (represented as \mathbf{c} channels) to each tile (pixel) within any set of contiguous $\mathbf{h} \times \mathbf{w}$ tiles (pixels) forms an $\mathbf{h} \times \mathbf{w} \times \mathbf{c}$ -dimensional image-like representation of the geographic location represented by the $\mathbf{h} \times \mathbf{w}$ tiles, as shown in Figure 1. A *count-based raster map* (CRM) is a single-channel representation ($\mathbf{c} = 1$) where the value of each pixel is the number of occurrences of GPS records in the zoom-24 tile corresponding to the pixel counted over all trajectories in $\mathcal{T}(t_0, \Delta t)$. Instead, if the occurrences of records per pixel is bucketed based on the direction in which the record was heading into 12 buckets of 30° , and each bucket is represented as an individual channel ($\mathbf{c} = 12$), we obtain the *heading count-based raster map* (HCRM) representation. Similarly, if the occurrences of records per pixel are bucketed based on the speed of the GPS records into 14 buckets of 5 miles per hour starting from 0, and each bucket is represented as an individual channel ($\mathbf{c} = 14$), we obtain the *speed-count* (SC) representation. If pixel values are set to the reachability embeddings of the corresponding zoom-24 tile, we obtain the \mathbf{d}_R -channel reachability embeddings representation. In contrast to LAR, reachability embeddings are *global* pixel-level representations — representation of tile \mathbf{s} depends on all activity in $\mathbf{N}_s^{\delta R}$. Trajectory-independent, road geometry related information is supplied using the *road network presence* (RNP) channel ($\mathbf{c} = 1$) which is a binary representation of the road network as a raster image where each pixel is assigned the value 1 if the corresponding zoom-24 tile has a road segment present and the value 0 otherwise. In this paper, $\mathbf{h} = \mathbf{w} = 256$.

Analogous to spectral imaging for remote sensing, where channels corresponding to different spectral bands capture additional information of a geographic location to complement their RGB (visible spectrum) counterparts, CRM, HCRM, SC, and reachability-based channels are multi-channel, image-like representations of information of the location deduced from trajectory data. The RNP channel can be considered as an *ontological* representation (where traffic *should* exist) of \mathbf{G}_{ES} while trajectory datasets are the *epistemological* representation (where traffic *actually* exists) of \mathbf{G}_{ES} .

6 Experiments and Results

The impact of reachability embeddings is evaluated on the performance of supervised, pixel-wise, semantic segmentation models for five downstream geospatial tasks, viz. (i) detection of overpasses, (ii) detection

⁴Probe data is similar to publicly available GPS trajectory datasets such as [33, 49]. More details can be found in the section titled “Probe data and privacy” in [36].

⁵Geospatial feature coordinates are suitably buffered to obtain WKT polygons. Assigning value 1 to pixels inside and 0 to those outside the polygons yields labels for semantic segmentation.

of pedestrian crosswalks, (iii) detection of driving access (entry/exit) points, (iv) detection of locations with traffic lights, and (v) detection of locations with stop signs. For all tasks, the UNet [40] architecture is trained to minimize the pixel-wise binary cross-entropy (BCE) between the predicted segmentation map and labels. A 60-20-20 randomly chosen training-validation-testing set is created and fixed for all subsequent experimentation.

Since reachability embeddings encode spatial connectivity (frequency and directionality of transitions) and speed (distance covered and time taken), baseline models using a combination (best model obtained after ablation study) of LAR-based channels as inputs are compared to the same model trained by replacing all LAR-based channels with reachability embeddings-based channels. Direct comparison between (i) models using inputs accounting for spatial connectivity versus inputs that do not, and (ii) the proposed self-supervised, learned representations versus explicit encoding of different aspects of trajectory data, demonstrates that learning more informative representations like reachability embeddings lead to better performance on downstream supervised tasks while using lesser trajectory data (i.e., reduced observation intervals, Δt). Probe data-based trajectory sets filtered for driving ($\mathcal{T}^d(t_0, \Delta t)$) and walking ($\mathcal{T}^w(t_0, \Delta t)$) motion modalities are obtained. Reachability embeddings (RE) are generated for both walking and driving modalities and denoted by WRE and DRE, respectively. CRM is also computed for both walking and driving modalities and denoted by WCRM and DCRM, respectively. HCRM and SC are calculated only for driving modality. It must be emphasized that all models built for the downstream tasks use only trajectory-based representations and/or RNP as input. No inputs from other remote sensing modalities (e.g., satellite imagery, SAR, LiDAR) are used since the goal of experiments in this section is to assess image-like representations of trajectory data for solving geospatial tasks as opposed to building the best model (which may combine multimodal inputs) for a given task.

Table 1: Combination of LAR-based channels identified from ablation study for the best baseline model for the downstream tasks. Corresponding inputs for reachability-based models.

Application	Baseline Models					Models w/ RE		
	RNP	DCRM	WCRM	HCRM	SC	RNP	DRE	WRE
Overpass	×	×	×	✓	×	×	✓	×
Crosswalk	×	✓	✓	×	×	×	✓	✓
Access Point	✓	×	×	✓	×	✓	✓	×
Traffic Lights	✓	✓	×	✓	✓	✓	✓	×
Stop Signs	✓	✓	✓	✓	✓	✓	✓	✓

Baselines for each downstream task: An ablation study is performed over all 31 possible combinations of RNP, DCRM, WCRM, HCRM, and SC to identify

the best combination of LAR-based input channels to build the baseline model for each task. Each input combination is concatenated along the channel dimension. Inputs are log-normalized so as to avoid spurious effects of the large dynamic range owing to the lack of an upper bound on the pixel-values. Hyperparameters are tuned on the validation set. Once trained, segmentation map predictions from all 31 models for each task is obtained for all examples of the test set. For every task, using ground truth labels available for the test set, the mean precision-recall curve (PRC) and the area under the curve (AUPRC) over all test examples is obtained for each of the 31 models by varying the confidence threshold of the binary segmentation outputs. The combination of LAR-based input representations that yield the highest AUPRC for each task is chosen as the baseline model for that task and is documented in Table 1.

Experiments with reachability embeddings:

With the goal of assessing the importance of self-supervised representations that account for various aspects of spatial connectivity (transition frequency, time, and distance), reachability-based models, documented in Table 1, are built that directly correspond to the baseline models by simply replacing any combination of DCRM, HCRM, and SC channels with DRE and replacing WCRM with WRE. Two variants each of the reachability-based models and baseline models are compared: reachability-based models that use DRE and WRE computed from trajectories observed within $[t_0, t_0 + \Delta t]$ with varying embedding sizes (a) $d_R = 8$ and (b) $d_R = 16$; baseline models using LAR-based as inputs computed using trajectories observed within (c) $[t_0, t_0 + \Delta t]$ and (d) $[t_0, t_0 + 3\Delta t]$. Since LAR are frequency counts of GPS records which can be noisy, increasing the observation time interval is a proxy-method to increase the signal-to-noise ratio (SNR) of the LAR-based channels. Increasing d_R allows the contractive autoencoder, \mathcal{F}_R , to retain more semantically meaningful information that may be helpful for the reconstruction task. Since larger d_R results in lowering the maximum possible batch-size (governed by GPU memory) for training models, we refrain from increasing d_R beyond 16 given the practical constraints of heterogeneous compute clusters having GPUs with varied memory.

Impact of reachability embeddings: Table 2 shows the quantitative comparison of the performance for all 5 downstream tasks, quantified using AUPRC on the test set after model training converges (50 epochs), between the two variants each of baseline and reachability-based models. Figure 3 shows the corresponding precision-recall curves. Three key observations emerge: (i) increasing the observation interval (increasing SNR) for computing LAR and increasing d_R increases

Table 2: Comparison of AUPRC (\uparrow is better) obtained from both variants of LAR and reachability-based models for 5 downstream geospatial tasks. Percentage gain compared to first row shown in brackets.

Input Channels	Observation Interval	Overpass Detection	Crosswalk Detection	Access Point Detection	Traffic Lights Detection	Stop Signs Detection
LAR Baseline	Δt	0.782	0.922	0.663	0.890	0.921
LAR Baseline	$3\Delta t$	0.785 (+0.4%)	0.923 (+0.1%)	0.684 (+3.0%)	0.925 (+3.8%)	0.924 (+0.3%)
Reachability, $d_R = 8$	Δt	0.899 (+15.0%)	0.959 (+4.0%)	0.843 (+21.4%)	0.974 (+8.6%)	0.938 (+1.9%)
Reachability, $d_R = 16$	Δt	0.925 (+18.3%)	0.976 (+5.9%)	0.864 (+23.3%)	0.985 (+9.6%)	0.959 (+4.1%)

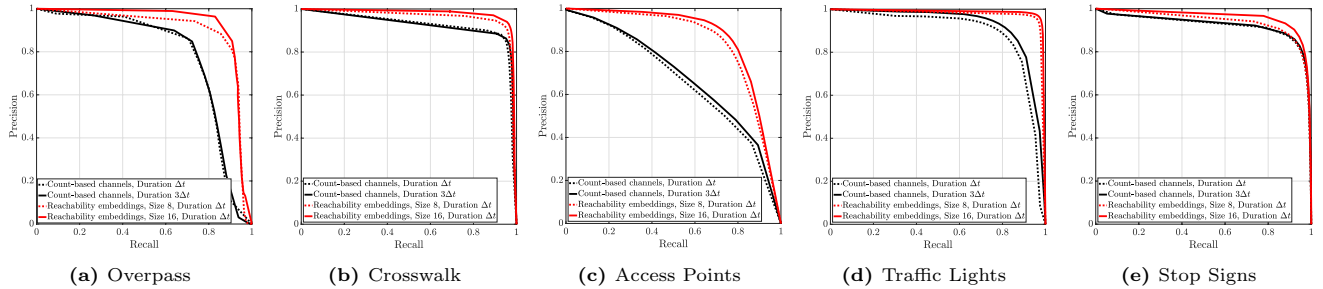


Figure 3: Precision-Recall curves obtained from both variants of LAR and reachability-based models for the 5 downstream tasks.

AUPRC — for most values of recall, precision increases due to reduction in false positives; (ii) reachability-based models outperform the baseline models, including those using LAR computed by observing 3 times more trajectories: the AUPRC gain by the inferior reachability-based model ($d_R = 8$) over the superior baseline model (observation interval $3\Delta t$) varies from 1.6% for stop signs detection task to 18.4% for the access point detection task; (iii) for the same observation time interval, Δt , simply replacing the LAR-based inputs by reachability embeddings ($d_R = 16$) results in a AUPRC gain that varies from 4.1% for the stop signs detection task to 23.3% for the access point detection task. These observations conclusively demonstrate that reachability embeddings are more informative, denser representations of trajectory data requiring lesser trajectories (upto 67% less) to compute. Thus, reachability embeddings may be used to compute semantically meaningful representations of trajectories in geographical areas with less traffic or to build computer vision-based models for low-resource geospatial tasks. A visual demonstration of the semantics captured by reachability embeddings is shown by the UMAP projection of embeddings computed in a large geographical area in Figure 5 in Supplementary Materials Section F. Visualizations of labels and predictions from reachability-based semantic segmentation models for three tasks is shown in Figure 6 in Supplementary Materials Section G.

7 Conclusions and Future Work

In this paper, we propose reachability embeddings, a novel, self-supervised method to learn representations of geographic locations (zoom-24 tiles modeled as nodes of ESG) from observed GPS trajectories (modeled as

Markovian paths in ESG). Reachability summaries for each node are image-like representations that capture the reachability pattern based on evidence from observed trajectories of the inflow (emission transitions) and outflow (absorption transitions) of traffic at the node. Summaries are compressed to a vector representation for each node, called reachability embeddings, using the encoder of a contractive, fully-convolutional autoencoder trained to reconstruct reachability summaries. Reachability summary generation and its contractive reconstruction can together be viewed as the pretext task to obtain reachability embeddings. Supplementary Materials Section E provides the theoretical motivation and a mathematical interpretation of reachability embeddings using the Chapman-Kolmogorov equations. The contractive regularization incentivizes robustness and invariance of embeddings to small perturbations in the summary leading embeddings of similar locations being close to each other (demonstrated by the UMAP projection of embeddings) in the learned, low-dimensional manifold. The proposed scalable, distributed algorithm (Algorithm 1) to generate reachability summaries, encoding spatial connectivity along with distance travelled and time taken during node transitions, shows good strong-scaling performance. Experiments in Section 6 confirm that reachability embeddings are more informative and denser (uses up to 67% less trajectory data compared to LAR) representations of geographic locations derived entirely from trajectory data leading to gains of 4–23% in AUPRC on five different downstream supervised prediction tasks.

Reachability embeddings facilitate multimodal learning in geospatial computer vision with spatiotemporal mobility data as one of the modes. Comparing versions of embeddings computed by varying t_0 , Δt , or both can

be used for detecting changes in geospatial features over time, identifying locations with timed turn restrictions or road closures, identifying seasonal patterns, etc. As evidenced in this work, self-supervision is a promising approach to analyze spatiotemporal trajectory datasets.

References

- [1] Y. BENGIO ET AL., *Representation learning: A review and new perspectives*, arXiv:1206.5538, (2014).
- [2] T. B. BROWN ET AL., *Language models are few-shot learners*, arXiv preprint arXiv:2005.14165, (2020).
- [3] H. CAI ET AL., *A comprehensive survey of graph embedding: Problems, techniques, and applications*, arXiv:1709.07604, (2018).
- [4] H. CAO ET AL., *Habit2vec: Trajectory semantic embedding for living pattern recognition in population*, IEEE Trans. Mob. Comp., 19 (2019), pp. 1096–1108.
- [5] S. CAO ET AL., *Deep neural networks for learning graph representations*, in AAAI, 2016.
- [6] T. CHEN ET AL., *A simple framework for contrastive learning of visual representations*, in ICML, 2020.
- [7] A. CRIVELLARI ET AL., *From motion activity to geo-embeddings: Generating and exploring vector representations of locations, traces and visitors through large-scale mobility data*, ISPRS IJGI, 8 (2019), p. 134.
- [8] D. WANG ET AL., *Big trajectory data mining: A survey of methods and applications*, Sensors, 20 (2020).
- [9] S. DABIRI ET AL., *Semi-supervised deep learning approach for transportation mode identification using GPS trajectory data*, IEEE TKDE, 32 (2019), pp. 1010–1023.
- [10] J. DEVLIN ET AL., *BERT: Pre-training of deep bidirectional transformers for language understanding*, arXiv:1810.04805, (2018).
- [11] C. DOERSCH ET AL., *Unsupervised visual representation learning by context prediction*, arXiv:1505.05192, (2015).
- [12] J. DONAHUE ET AL., *Large scale adversarial representation learning*, arXiv:1907.02544, (2019).
- [13] Y. DONG ET AL., *Scalable representation learning for heterogeneous networks*, in ACM SIGKDD, 2017.
- [14] EPSG GEODETIC PARAMETER REGISTRY, *EPSG:3857*. <https://epsg.io/3857>.
- [15] S. GANGULI ET AL., *GeoGAN: A conditional GAN with reconstruction and style loss to generate standard layer of maps from satellite images*, arXiv:1902.05611, (2019).
- [16] Q. GAO ET AL., *Identifying human mobility via trajectory embeddings*, in IJCAI, 2017.
- [17] S. GIDARIS ET AL., *Unsupervised representation learning by predicting image rotations*, in ICLR, 2018.
- [18] S. GIDARIS ET AL., *Learning representations by predicting bags of visual words*, in CVPR, 2020.
- [19] I. J. GOODFELLOW ET AL., *Generative adversarial networks*, arXiv:1406.2661, (2014).
- [20] A. GRAMA ET AL., *Introduction to parallel computing*, Pearson Education, 2003.
- [21] J. GRILL ET AL., *Bootstrap your own latent: A new approach to self-supervised learning*, in NeurIPS, 2020.
- [22] A. GROVER ET AL., *node2vec: Scalable feature learning for networks*, in ACM SIGKDD, 2016.
- [23] K. HE ET AL., *Momentum contrast for unsupervised visual representation learning*, arXiv:1911.05722, (2019).
- [24] C. V. K. IYER ET AL., *Trinity: A no-code AI platform for complex spatial datasets*, arXiv:2106.11756, (2021).
- [25] X. JIANG ET AL., *TrajectoryNet: An embedded GPS trajectory representation for point-based classification using RNNs*, arXiv:1705.02636, (2017).
- [26] L. JING ET AL., *Self-supervised visual feature learning with deep neural networks*, arXiv:1902.06162, (2017).
- [27] D. P. KINGMA ET AL., *Auto-encoding variational Bayes*, arXiv:1312.6114, (2013).
- [28] J. LESKOVEC ET AL., *Mining of massive data sets*, Cambridge University Press, 2020.
- [29] X. LIU ET AL., *Self-supervised learning: Generative or contrastive*, arXiv:2006.08218, (2020).
- [30] Z. LIU ET AL., *Semantic proximity search on heterogeneous graph by proximity embedding*, in AAAI, 2017.
- [31] L. MA ET AL., *Deep learning in remote sensing applications: A meta-analysis and review*, ISPRS JPRS, 152 (2019), pp. 166–177.
- [32] T. MIKOLOV ET AL., *Efficient estimation of word representations in vector space*, arXiv:1301.3781, (2013).
- [33] L. MOREIRA-MATIAS ET AL., *Predicting taxi-passenger demand using streaming data*, IEEE Trans. Intelligent Transportation Sys., 14 (2013), pp. 1393–1402.
- [34] M. NOROOZI ET AL., *Unsupervised learning of visual representations by solving jigsaw puzzles*, ECCV, (2016).
- [35] OPENSTREETMAP, *Public GPS Traces*. <https://www.openstreetmap.org/traces>.
- [36] M. PANZARINO, *Apple is rebuilding Maps from the ground up*, TechCrunch, (2018).
- [37] A. PEREZ ET AL., *Semi-supervised multitask learning on multispectral satellite images using Wasserstein Generative Adversarial Networks (GANs) for predicting poverty*, arXiv:1902.11110, (2019).
- [38] B. PEROZZI ET AL., *Deepwalk: Online learning of social representations*, in ACM SIGKDD, 2014.
- [39] S. RIFAI ET AL., *Contractive auto-encoders: Explicit invariance during feature extraction*, in ICML, 2011.
- [40] O. RONNEBERGER ET AL., *U-Net: CNNs for biomedical image segmentation*, arXiv:1505.04597, (2015).
- [41] C. D. SMITH ET AL., *Incorporating GIS and technology in response to COVID-19*, Prev. Chronic Dis., 17 (2020).
- [42] A. SOLOMON ET AL., *Predict demographic information using word2vec on spatial trajectories*, in UMAP, 2018.
- [43] D. STIRZAKER ET AL., *Probability and random processes*, Clarendon Press, 1992.
- [44] P. VINCENT ET AL., *Extracting and composing robust features with denoising autoencoders*, in ICML, 2008.
- [45] D. WANG ET AL., *Structural deep network embedding*, in ACM SIGKDD, 2016.
- [46] WIKIPEDIA, *Haversine formula*. <http://w.wiki/4Aj7>.
- [47] WIKIPEDIA, *Well-known text*. <https://w.wiki/4Aj8>.
- [48] X. XIAO ET AL., *VAE-Info-cGAN: Generating synthetic images by combining pixel-level and feature-level geospatial conditional inputs*, arXiv:2012.04196, (2020).

- [49] J. YUAN ET AL., *T-Drive: Driving directions based on taxi trajectories*, in ACM SIGSPATIAL, 2010.
- [50] Y. ZHENG, *Trajectory data mining: An overview*, ACM TIST, 6 (2015), pp. 1–41.
- [51] J. ZHOU ET AL., *Graph neural networks: A review of methods and applications*, arXiv:1812.08434, (2018).

Supplementary Materials

A Distributed, data-parallel implementation of Algorithm 1

Algorithm 2 presents the pseudo-code of a distributed, data-parallel implementation of Algorithm 1 written using the Scala Dataset API in Apache Spark⁶ syntax. Apache Spark is an open-source, fault-tolerant, distributed, and data parallel cluster computing framework with support for distributed in-memory computation.

Algorithm 2 Distributed, data-parallel implementation of Algorithm 1 for generating $\Psi_s^{ea} \forall s \in \bar{V}_{ES}$

Input: $\mathcal{T}_{t_0+\Delta t} = \{\mathbf{T}_1 \dots \mathbf{T}_M\}$, $|\mathbf{T}_i| = n_i \forall i \in [1, M]$,
 $\mathbf{T}_i = \{\mathbf{p}_1^i, \dots, \mathbf{p}_{n_i}^i\}$ where $\mathbf{p}_k^i = \{z_k^i, t_k^i\}$

Output: $\Psi_s^e, \Psi_s^a \forall s \in \bar{V}_{ES}$

Parameters: δ_R

Initialize: Ingest $\mathcal{T}_{t_0+\Delta t}$ as trj

```

1: procedure ReachabilitySummaryGenerator()
2:   result = trj.flatMap(t ⇒ createAPairs(t))
3:   .flatMap(p ⇒ createEPairs(p))
4:   .map(p ⇒ getIdxForDestinationTile(p))
5:   .map(p ⇒ (p.cTile, p.dIdx, p.flg) → p.cnt)
6:   .reduceByKey((v1, v2) ⇒ v1 + v2)
7:   .map((k, v) ⇒ k.cTile → (k.dIdx, k.flg, v))
8:   .groupByKey()
9:   .map((k, v) ⇒ Create  $\Psi_k^e, \Psi_k^a, \Psi_k^{ea}$  for tile k)
10:  .saveToDistributedStorage( $\Psi_k^{ea} \forall k \in \bar{V}_{ES}$ )
11: function createAPairs( $\mathbf{T}_i$ )
12:   for  $k \leftarrow 1$  to  $n_i$  do
13:     for  $l \leftarrow k$  to  $n_i$  do
14:       if  $z_l^i \in N_{z_k^i}^{\delta_R}$  then
15:         return Pair( $z_k^i, z_l^i, 'a', 1.0$ )
16: function createEPairs(p: Pair)
17:   return (p, Pair(p.node2, p.node1, 'e', p.cnt))
18: function getIdxForDestinationTile(p: Pair)
19:    $s, s' \leftarrow p.node1, p.node2$ 
20:    $\text{rmIdx} \leftarrow L(\mathbf{x}_{s'} - \mathbf{x}_s + \delta_R) + (\mathbf{y}_{s'} - \mathbf{y}_s + \delta_R)$ 
21:   return IdxPair(p.node1, rmIdx, p.flg, p.cnt)

```

Adopting an object-oriented style, Algorithm 2 uses the Pair and IdxPair case classes defined as follows. A transition between two nodes is represented by the Pair object that has four parameters: (i) node1 and node2 denote the nodes involved; (ii) flg denotes the type of transition from the vantage point of node1 and is set to flg='a' for the transition node1→node2 while it is set to flg='e' for the node2→node1 transition; (iii) cnt, initialized to 1.0, that counts the number of occurrences of the transition. An IdxPair object also represents a

transition between two nodes, $s, s' \in \bar{V}_{ES}$, and has four parameters: (i) node is one of s or s' ; (ii) rmIdx is the row-major index of s' in Ψ_s^a if node= s while it is the row-major index of s in $\Psi_{s'}^e$ if node= s' ; (iii) flg is a flag set to 'a' if node= s and to 'e' if node= s' , (iv) cnt is the frequency of the observed transition.

Line 2 of Algorithm 2 creates valid absorption transitions as Pair objects from \mathbf{T}_i . Line 3 computes the corresponding emission transition for every absorption transition. All Pair objects representing emission and absorption transitions are converted to corresponding IdxPair objects in line 4. Lines 5 and 6 count the observed frequency of both absorption and emission transitions between all pairs of nodes in \bar{V}_{ES} from all trajectories in $\mathcal{T}(t_0, \Delta t)$. All associated transitions are gathered in line 8 to compute the absorption and emission channels which are concatenated in line 9 to obtain the reachability summaries for all nodes in \bar{V}_{ES} . Line 10 saves the output into distributed storage.

Algorithm 3 Encode distance & time weighting in Ψ_s^{ea}

Input: $\mathbf{T}_i \in \mathcal{T}_{t_0+\Delta t}$, $|\mathbf{T}_i| = n_i$, $\mathbf{T}_i = \{\mathbf{p}_1^i, \dots, \mathbf{p}_{n_i}^i\}$
 where $\mathbf{p}_k^i = \langle z_k^i, t_k^i \rangle$

Output: Map \mathbf{S}

Parameters: $\delta_R, \sigma_d, \sigma_t$

Initialize: $\mathbf{T}_i = \{\bar{\mathbf{p}}_1^i, \dots, \bar{\mathbf{p}}_{n_i}^i\}$ such that the 3-tuple
 $\bar{\mathbf{p}}_k^i = \langle z_k^i, t_k^i, d_k^i = 0 \rangle \forall \mathbf{T}_i \in \mathcal{T}_{t_0+\Delta t}$

```

1: function analyzeTrajectories( $\mathcal{T}_{t_0+\Delta t}$ )
2:   Initialize map  $\mathbf{S} = \emptyset$ 
3:   for trajectory  $\mathbf{T}_i \in \mathcal{T}_{t_0+\Delta t}$  do
4:     for  $k \leftarrow 2$  to  $n_i$  do ▷  $\mathcal{O}(n_i)$ 
5:        $\Delta d = \text{haversineDistance}(z_{(k-1)}^i, z_k^i)$ 
6:        $d_k^i \leftarrow d_{(k-1)}^i + \Delta d$ 
7:     for  $k \leftarrow 1$  to  $n_i$  do
8:       for  $l \leftarrow k$  to  $n_i$  do
9:         if  $z_l^i \in N_{z_k^i}^{\delta_R}$  then
10:          if  $z_k^i \notin \mathbf{S}$ ,  $\mathbf{S}[z_k^i] = \{\mathbf{S}_{z_k^i}^e, \mathbf{S}_{z_k^i}^a = \emptyset\}$ 
11:          if  $z_l^i \notin \mathbf{S}$ ,  $\mathbf{S}[z_l^i] = \{\mathbf{S}_{z_l^i}^e, \mathbf{S}_{z_l^i}^a = \emptyset\}$ 
12:           $r_{z_k^i}(z_l^i) \leftarrow \text{getIndex}(z_k^i, z_l^i)$ 
13:           $r_{z_l^i}(z_k^i) \leftarrow \text{getIndex}(z_l^i, z_k^i)$ 
14:           $\Delta_{d,i}^{(z_k^i, z_l^i)} \leftarrow (d_l^i - d_k^i)$ 
15:           $\Delta_{t,i}^{(z_k^i, z_l^i)} \leftarrow (t_l^i - t_k^i)$ 
16:           $\Delta \mathbf{w}(z_k^i, z_l^i; \sigma_d, \sigma_t) \leftarrow \text{Section (4.3)}$ 
17:           $c_{z_k^i}^a(z_l^i) = \Delta \mathbf{w}(z_k^i, z_l^i; \sigma_d, \sigma_t)$ 
18:           $c_{z_l^i}^e(z_k^i) = \Delta \mathbf{w}(z_l^i, z_k^i; \sigma_d, \sigma_t)$ 
19:           $\mathbf{S}_{z_k^i}^a[r_{z_k^i}(z_l^i)] += c_{z_k^i}^a(z_l^i)$ 
20:           $\mathbf{S}_{z_l^i}^e[r_{z_l^i}(z_k^i)] += c_{z_l^i}^e(z_k^i)$ 
21:   return  $\mathbf{S}$ 

```

⁶<https://spark.apache.org/>

B Modified analyzeTrajectories procedure

Algorithm 3 presents the modified version of `analyzeTrajectories` procedure when distance and time weighting, discussed in Section 4.3, are used. Note that the same transition, $(\mathbf{s}, \mathbf{s}')$, can have different counts within a single trajectory if the transitions take two different possible paths during which the distance covered and time taken to cover the distance are different. Line 5 in Algorithm 3 uses the haversine formula [46] to calculate the great-circle distance between the centroids of two zoom-24 tiles. One can analogize the weight decays for nodes $\mathbf{s}' \in \mathbf{N}_s^{\delta_R}$ in the reachable neighborhood of node \mathbf{s} to the soft-attention mechanism in NLP where the magnitude of the weight decay can be thought of as the ‘‘attention’’ paid by node \mathbf{s} to the node \mathbf{s}' in the calculation of the reachability summary, Ψ_s^{ea} .

C T-Drive Dataset Pre-processing

To demonstrate scalability of Algorithm 1 in Section 4.4, the publicly available T-Drive dataset [49] from Microsoft Research, containing location coordinates (latitude-longitude pairs) and timestamps for 7 days of 10,357 taxis in Beijing, is used. To transform these into a trajectory dataset, $\mathcal{T}(t_0, \Delta t)$, the data is pre-processed so that the daily chronological sequence of coordinate-timestamp pairs for each taxi is considered as one contiguous trajectory leading to $|\mathcal{T}(t_0, \Delta t)| = M = 68,851$, where $t_0 = \text{February } 02, 2008$ and $\Delta t = 7$ days. Coordinates are converted to zoom-24 tiles to match the format required for consumption by Algorithm 1. Three datasets of 2000, 8000, and 64000 trips are randomly sampled from this processed dataset for the strong scaling [20] analysis performed in Section 4.4.

D The Contractive Autoencoder

The details of the neural architecture of the contractive autoencoder, \mathcal{F}_R , are presented in Figure 4. The encoder, \mathcal{F}_R^e , has 5.2 million trainable parameters and the decoder, \mathcal{F}_R^d , has 5.8 million parameters, respectively. Using cross-validation, λ in equation (4.5c) is found to be 0.5. The autoencoder is implemented and trained using the Python API for TensorFlow. Distributed training of the model uses 8 NVIDIA Tesla V100 GPUs with a batch-size of 256 examples per GPU. Reachability embeddings may be viewed as a mapping of a geographic location (e.g., described by a $\mathbf{h} \times \mathbf{w} \times 3$ satellite image with zoom-24 tiles as pixels) to an *embedding field* (described by $\mathbf{h} \times \mathbf{w} \times \mathbf{d}_R$ parameters) based on observed mobility in that geographic location over a specified observation interval. Reachability embeddings can also be used along with other multi-channel representations of GPS trajectories (e.g., LAR-based representations) or other

data modalities (e.g., SAR, aerial imagery, multispectral and hyperspectral satellite imagery) to solve downstream geospatial prediction tasks.

E Interpreting Reachability Embeddings using the Chapman-Kolmogorov Equations

The Markovian transitions in \mathbf{V}_{ES} define a *transition probability matrix* [43], $\mathbf{P}_{ES} = [\mathbb{P}_{ES}^{(s,s')}] \in [0, 1]^{|V_{ES}| \times |V_{ES}|}$, where,

$$\mathbb{P}_{ES}^{(s,s')} = \frac{\mathbf{w}_{ES}^{(s,s')}}{\sum_{s'' \in V_{ES}} \mathbf{w}_{ES}^{(s,s'')}} \quad \forall \mathbf{s}, \mathbf{s}' \in V_{ES}. \quad (\text{E.1})$$

Matrices, Ψ_s^e and Ψ_s^a , defined in equations (4.4a) and (4.4b), are closely related to the transition probability matrix, \mathbf{P}_{ES} . For any square matrix, X , let $\text{sum}(X)$ denote the sum of all the matrix elements and $\text{scale}(X) = X/\text{sum}(X)$. Then, $\text{scale}(\Psi_s^e)$ and $\text{scale}(\Psi_s^a)$ are spatial proximity-preserving rearrangements in matrix form of the column and row vectors of \mathbf{P}_{ES} corresponding to node \mathbf{s} , respectively.

The Chapman-Kolmogorov equations (CKE) [43] are a fundamental identity of Markov chains and the inspiration for the construction of reachability summaries described in section 4.1. While CKE is a more general result, in this paper we consider the specific case of *discrete* and *homogeneous* [43] Markov chains.

THEOREM E.1. (CHAPMAN-KOLMOGOROV EQUATIONS)

For a discrete and homogeneous⁷ Markov chain, $\mathbf{X} = \{X_0, X_1, \dots\}$, with countably finite state space, \mathbf{S} , and transition probability matrix, \mathbf{P} , let $\mathbf{P}^{(n)} = [\mathbf{P}_{ij}^{(n)}]$ denote the n -step transition matrix which is the matrix of n -step transition probabilities, $\mathbf{P}_{ij}^{(n)} = \mathbb{P}(X_n = j | X_0 = i)$, $i, j \in \mathbf{S}$. Then, $\forall i, j \in \mathbf{S}$, $n, k \in \mathbb{Z}^+$, and $0 \leq k \leq n$,

$$\mathbf{P}_{ij}^{(n)} = \sum_{z \in \mathbf{S}} \mathbf{P}_{iz}^{(k)} \mathbf{P}_{zj}^{(n-k)} \quad (\text{E.2a})$$

$$\implies \mathbf{P}^{(n)} = \mathbf{P}^{(k)} \mathbf{P}^{(n-k)}, \mathbf{P}^{(n)} = \mathbf{P}^n \quad (\text{E.2b})$$

Consider the state space \mathbf{V}_{ES} . All states are discrete and all Markovian transitions in the state space are modeled as homogeneous. For any node, \mathbf{s} , we wish to learn a representation of \mathbf{s} that captures its contribution to connecting any two arbitrarily chosen nodes $\mathbf{s}', \mathbf{s}'' \in \mathbf{V}_{ES}$. Specifically, we wish to encode the information captured by the two-step transition probability from \mathbf{s}' to \mathbf{s}'' passing through \mathbf{s} into the representation for \mathbf{s} , for all choices of $\mathbf{s}', \mathbf{s}'' \in \mathbf{V}_{ES}$ as evidenced by transitions deduced from observed trajectories in the set $\mathcal{T}(t_0, \Delta t)$.

⁷ $\mathbb{P}(X_m = j | X_{m-1} = i) = \mathbb{P}(X_1 = j | X_0 = i) \quad \forall i, j \in \mathbf{S}$ and $m \in \mathbb{Z}^+$, where $\mathbb{P}(E)$ denotes the probability of an event E .

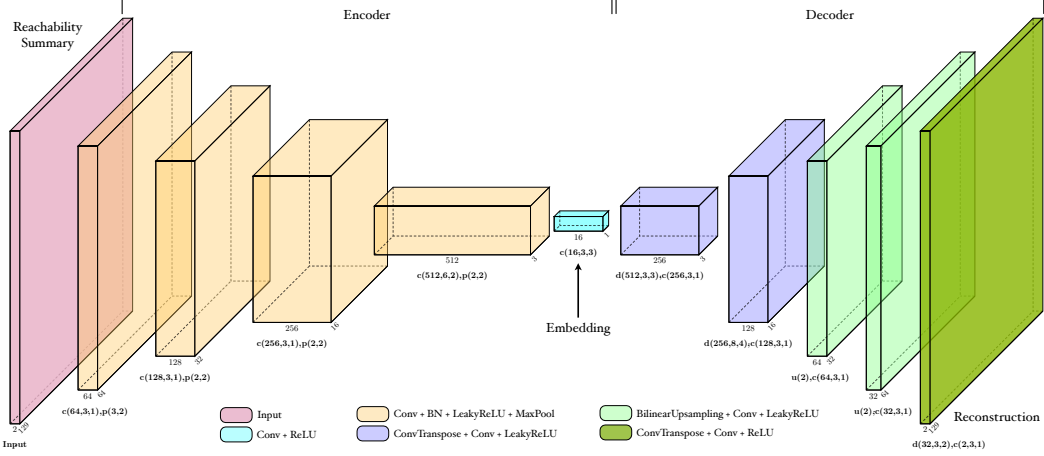


Figure 4: Contractive autoencoder architecture. Blocks describe outputs from preceding layer detailed in block caption. Layers denoted using $c(f, k, s)$, $p(k, s)$, $d(f, k, s)$, and $u(m)$, where, c is convolution, p is max-pooling, d is transposed convolution, $u(m)$ is bilinear upsampling with multiplicity factor m , f is number of filters, k is kernel size, and s is stride.

This is in contrast to algorithms like [13, 22, 38] which synthetically construct random walks on a graph.

Setting $k = 1, n = 2$, for chosen state $\mathbf{s} \in \mathbf{V}_{ES}$ and $\forall \mathbf{s}', \mathbf{s}'' \in \mathbf{V}_{ES}$, it follows from equation (E.2b) that

$$\left(\mathbf{P}_{ES}^{(\mathbf{s}', \mathbf{s}'')}\right)^2 = \mathbf{P}_{ES}^{(\mathbf{s}', \mathbf{s})} \mathbf{P}_{ES}^{(\mathbf{s}, \mathbf{s}'')} + \sum_{z \in \mathbf{V}_{ES} \setminus \{\mathbf{s}\}} \mathbf{P}_{ES}^{(\mathbf{s}', z)} \mathbf{P}_{ES}^{(z, \mathbf{s}'')} \quad (\text{E.3})$$

where the first term on the right-hand side, henceforth denoted as $C_s^{(\mathbf{s}', \mathbf{s}'')}$, measures the contribution of state \mathbf{s} to the total 2-step transition probability from state \mathbf{s}' to state \mathbf{s}'' . Note that only the subset of trajectories in $\mathcal{T}(t_0, \Delta t)$ that pass through \mathbf{s} , denoted as $\mathcal{T}(t_0, \Delta t)(\mathbf{s})$, contribute to $C_s^{(\mathbf{s}', \mathbf{s}'')}$. Summing $C_s^{(\mathbf{s}', \mathbf{s}'')}$ over all possible $\mathbf{s}', \mathbf{s}'' \in \mathbf{V}_{ES}$, which is the total contribution of \mathbf{s} to all transitions in \mathbf{V}_{ES} , denoted as C_s , we obtain

$$\begin{aligned} C_s &= \sum_{\mathbf{s}', \mathbf{s}'' \in \mathbf{V}_{ES}} C_s^{(\mathbf{s}', \mathbf{s}'')} = \sum_{\mathbf{s}' \in \mathbf{V}_{ES}} \mathbf{P}_{ES}^{(\mathbf{s}', \mathbf{s})} \sum_{\mathbf{s}'' \in \mathbf{V}_{ES}} \mathbf{P}_{ES}^{(\mathbf{s}, \mathbf{s}'')} \\ &= \sum_{\mathbf{s}' \in \Xi_s} \mathbf{P}_{ES}^{(\mathbf{s}', \mathbf{s})} \sum_{\mathbf{s}'' \in \Lambda_s} \mathbf{P}_{ES}^{(\mathbf{s}, \mathbf{s}'')} \end{aligned} \quad (\text{E.4})$$

If only transitions from $\mathbf{N}_s^{\delta R}$ are considered valid,

$$C_s = \sum_{\mathbf{s}' \in \Xi_s^{\delta R}} \mathbf{P}_{ES}^{(\mathbf{s}', \mathbf{s})} \sum_{\mathbf{s}'' \in \Lambda_s^{\delta R}} \mathbf{P}_{ES}^{(\mathbf{s}, \mathbf{s}'')} \quad (\text{E.5})$$

If the total number of Markovian transitions in $\mathcal{T}(t_0, \Delta t)(\mathbf{s})$ that start at \mathbf{s} is ν_s^a , and that end at \mathbf{s}

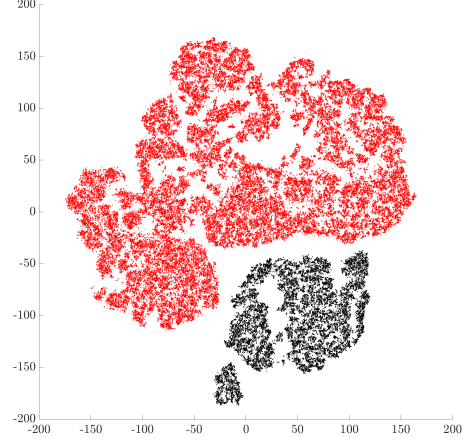


Figure 5: UMAP of embeddings in a chosen geographic location: nodes on highways (black), otherwise (red).

is ν_s^e , we have

$$\begin{aligned} \nu_s^a \cdot \nu_s^e \cdot C_s &= \sum_{\mathbf{s}' \in \Xi_s^{\delta R}} \left(\nu_s^e \mathbf{P}_{ES}^{(\mathbf{s}', \mathbf{s})}\right) \sum_{\mathbf{s}'' \in \Lambda_s^{\delta R}} \left(\nu_s^a \mathbf{P}_{ES}^{(\mathbf{s}, \mathbf{s}'')}\right) \\ &= \boldsymbol{\psi}_s^{eT} \boldsymbol{\psi}_s^a \end{aligned} \quad (\text{E.6})$$

Here, $\boldsymbol{\psi}_s^e$ and $\boldsymbol{\psi}_s^a$ are L^2 -dimensional column vectors of the emission and absorption probabilities of \mathbf{s} corresponding to the L^2 states in $\mathbf{N}_s^{\delta R}$.

When $\boldsymbol{\psi}_s^e$ and $\boldsymbol{\psi}_s^a$ are reshaped to spatial-relation-preserving $L \times L$ -dimensional matrices based on the relative positions of the nodes in $\mathbf{N}_s^{\delta R}$ on the earth surface graph, \mathbf{G}_{ES} , they yield $\boldsymbol{\Psi}_s^e$ and $\boldsymbol{\Psi}_s^a$, respectively. In other words, the emission and absorption channels exactly capture the contribution of node \mathbf{s} to connecting nodes in its reachable neighborhood where it acts as the intermediary, thereby capturing essential spatial

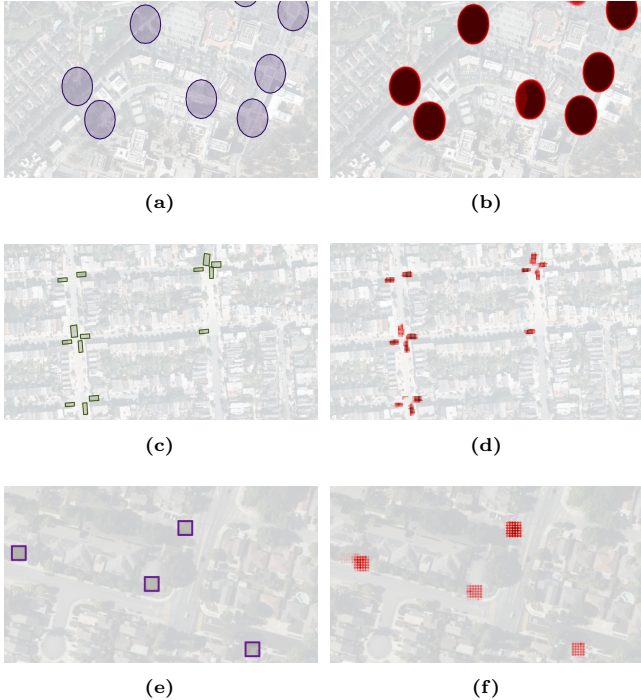


Figure 6: Examples of labels (subfigures (a), (c), (e)) and semantic segmentation model predictions from reachability-based models (subfigures (b), (d), (f)) on the test set for 3 downstream tasks. Subfigures (a) and (b) are show labels and predictions for traffic lights, subfigures (c) and (d) are show labels and predictions for stop signs, and subfigures (e) and (f) show labels and predictions for access points. Satellite imagery is superposed for visual reference only.

connectivity information. One can analogize this to the role layover airports or connection hubs play (e.g., Dubai for Emirates, Munich for Lufthansa) in 1-stop flights. The key idea is to use the information of the set of flights flying *into* the airport and the information of the set of flights flying *out of* the airport to learn the representation of the layover airport.

With the interpretation of C_s developed above, we can sum both sides of equation (E.3) to obtain the sum of the two-step transition probability of the transition $s' \rightarrow s''$ for all choices of nodes $s, s' \in V_{ES}$, as

$$\begin{aligned}
 \sum_{s', s'' \in V_{ES}} \left(\mathbf{P}_{ES}^{(s', s'')} \right)^2 &= \sum_{z \in V_{ES}} \sum_{s', s'' \in V_{ES}} \mathbf{P}_{ES}^{(s', z)} \mathbf{P}_{ES}^{(z, s'')} \\
 &= \sum_{z \in V_{ES}} C_z \\
 &= \sum_{z \in V_{ES}} \boldsymbol{\psi}_z^{eT} \boldsymbol{\psi}_z^a
 \end{aligned} \tag{E.7}$$

In other words, equation E.7 reinterprets the Chapman-Kolmogorov identity from the lens of reachability-based emission and absorption channels.

F UMAP Projection of Reachability Embeddings

A good learned representation ensures, among other qualities, that similar entities have similar representations [1]. The contractive autoencoder, \mathcal{F}_R , produces robust neural encodings [39] of the reachability summary. This means that geographic locations with similar spatial connectivity patterns as observed from GPS trajectories have similar reachability embeddings. A visual demonstration of the semantics captured by reachability embeddings is shown by the UMAP projection of embeddings computed in a large geographical area in Figure 5. Points in black denote nodes associated with highways (mostly straight roads with few connections to neighbors) are clustered and cleanly separated from red points that denote nodes not associated with highways.

G Model Prediction Visualizations

Examples of labels and semantic segmentation model predictions from reachability-based models is shown for 3 downstream tasks, viz., detecting traffic lights, stop signs, and access points in Figure 6. The model predictions are pixel-wise (pixels are zoon-24 tiles) values between 0 (light red) and 1 (dark red). The labels and predictions are superposed on satellite imagery (reduced opacity for clarity of labels and predictions) only for visual reference.